USGS
science for a changing world

Chemical Characterization of San Andreas Fault Observatory at Depth (SAFOD) Phase 3 Core

Open-File Report 2023–1019

U.S. Department of the Interior
U.S. Geological Survey

Chemical Characterization of San Andreas Fault Observatory at Depth (SAFOD) Phase 3 Core

By Diane E. Moore and Kelly K. Bradbury

Open-File Report 2023–1019

U.S. Department of the Interior
U.S. Geological Survey

U.S. Geological Survey, Reston, Virginia: 2023

Suggested citation:
Moore, D.E., and Bradbury, K.K., 2023, Chemical characterization of San Andreas Fault Observatory at Depth (SAFOD) Phase 3 core: U.S. Geological Survey Open-File Report 2023–1019, 15 p., https://doi.org/10.3133/ofr20231019.

ISSN 2331-1258 (online)

Contents

Figures

Conversion Factors

International System of Units to U.S. customary units

Multiply	By	To obtain
	Length	
centimeter (cm)	0.3937	inch (in.)
millimeter (mm)	0.03937	inch (in.)
meter (m)	3.281	foot (ft)
meter (m)	1.094	yard (yd)
kilometer (km)	0.6214	mile (mi)

Datums

Vertical coordinate information is referenced to the North American Vertical Datum of 1988 (NAVD 88).

Horizontal coordinate information is referenced to the North American Datum of 1983 (NAD 83).

Altitude, as used in this report, refers to distance above the vertical datum.

Abbreviations

BSE	backscattered electron
CDZ	central deforming zone
EDS	energy-dispersive X-ray spectroscopy
LOI	loss on ignition
SAFOD	San Andreas Fault Observatory at Depth
SEM	scanning electron microscope
SDZ	southwest deforming zone
USGS	U.S. Geological Survey
XRF	X-ray fluorescence
µm	micrometer

Chemical Characterization of San Andreas Fault Observatory at Depth (SAFOD) Phase 3 Core

By Diane E. Moore[1] and Kelly K. Bradbury[2]

Abstract

We present new X-ray fluorescence compositions of 27 core samples from Phase 3, Hole G of the San Andreas Fault Observatory at Depth, nearly doubling the published dataset for the core. The new analyses consist of major and trace element compositions and the first published data for rare earth elements from Hole G. Whole-rock compositions were obtained to further the analysis of active geochemical processes within the creeping section of the San Andreas Fault in central California. In this report, we plot the new data along with previously published analyses to illustrate some of the compositional features of the Hole G core and to relate them to the core mineralogy.

Introduction and Dataset Description

The San Andreas Fault Observatory at Depth (SAFOD) deep drilling project successfully crossed the creeping section of the San Andreas Fault northwest of the town of Parkfield in central California (fig. 1*A*). The active trace of the San Andreas Fault lies within North American Plate rocks at SAFOD (Zoback and others, 2010, 2011), where the trace appears as an approximately (~) 200-meter-wide damage zone. Drilling operations were completed in three phases: the SAFOD Main Hole was drilled in Phases 1 (2004) and 2 (2005) (fig. 1*B*), and during Phase 3 (2007), sections of core were collected at three locations in sidetrack drilling operations. The first section, obtained from Hole E (labelled 1 in fig. 1*C*, *D*), sampled sedimentary rock units of the Salinian terrane. Spot coring in Hole G successfully sampled two creeping strands of the fault that were previously identified through well casing deformation of the main hole within the damage zone. The more slowly creeping southwest deforming zone (SDZ) is 1.6 meters (m) wide and marks the southwest boundary of the San Andreas Fault damage zone (see core section 2 in fig. 1*C*, *D*). The 2.6-meter-wide central deforming zone (CDZ), positioned in the middle of the damage zone where core section 3 was collected, accommodates most of the annual ~25 millimeters (mm) of creep that has been documented on this part of the San Andreas Fault (Titus and others, 2006, 2011). The core divisions and lithologies designated for Hole G core by Bradbury and others (2011) are shown at the tops of figures 2–6.

Whole-rock X-ray fluorescence (XRF) data for 39 samples from Hole G were previously published by Bradbury and others (2011, 2015) and Janssen and others (2014). This report expands the dataset to include 27 new XRF analyses comprising major, trace, and rare earth elements. This dataset is the first in Hole G to include rare earth elements. Sampling was concentrated at (1) the boundaries between the creeping traces and their adjoining rocks and (2) along meters-long sections of Hole G core that lacked chemical data. The analyses were performed at the Peter Hooper GeoAnalytical Laboratory at Washington State University in Pullman, Washington (https://environment.wsu.edu/facilities/geoanalytical-lab/). Major and trace element concentrations were measured by XRF techniques. Rare earth element and additional trace element concentrations were collected by inductively coupled plasma mass spectrometer techniques.

The compositions and their associated metadata are presented in the accompanying data release (Moore and Bradbury, 2021), which consists of two spreadsheets: (1) SAFOD Major & Trace Elements and (2) SAFOD Rare Earth & Trace Elements. The major elements, reported as weight percent oxides in the first spreadsheet, are SiO_2, TiO_2, Al_2O_3, FeO (total Fe), MnO, MgO, CaO, Na_2O, K_2O, and P_2O_5. The trace elements, reported in units of elemental parts per million, are Ni, Cr, Sc, V, Ba, Rb, Sr, Zr, Y, Nb, Ga, Cu, Zn, Pb, La, Ce, Th, Nd, and U. Also included in this first spreadsheet are SO_3, Cl, and loss on ignition (LOI) determinations (in weight percent). Repeat analyses (denoted by the letter "r") were carried out on two samples as a quality-control measure. The 27 elements in the second spreadsheet, reported in units of elemental parts per million, are La, Ce, Pr, Nd, Sm, Eu, Gd, Tb, Dy, Ho, Er, Tm, Yb, Lu, Ba, Th, Nb, Y, Hf, Ta, U, Pb, Rb, Cs, Sr, Sc, and Zr. Several of the trace elements were analyzed by both techniques and are included in both tables. No formal comparison of the duplicated data was made.

[1]U.S. Geological Survey.

[2]Utah State University.

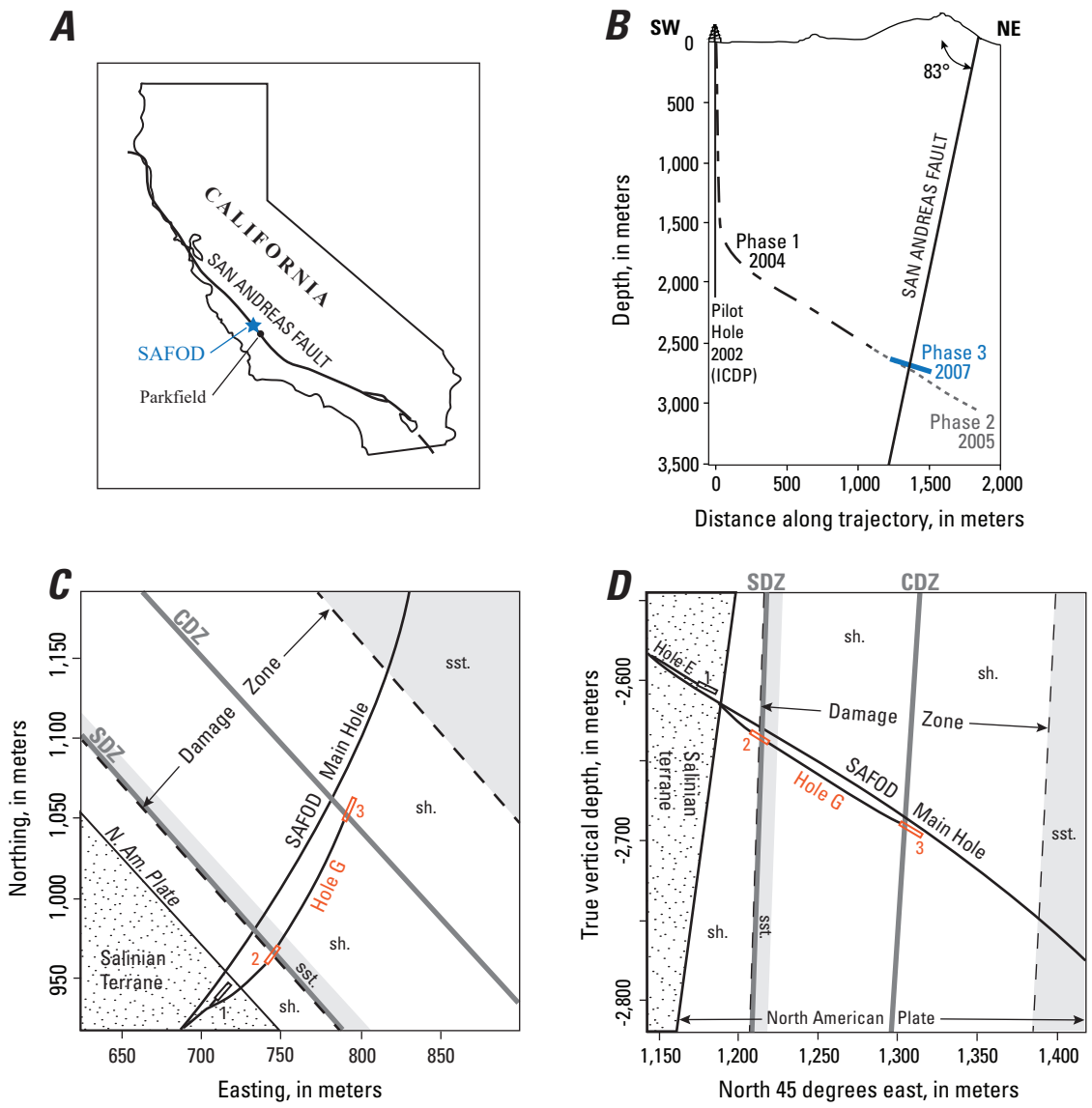

Figure 1. Overview of study sample locations at the San Andreas Fault Observatory at Depth (SAFOD). *A*, Map showing the location of SAFOD in California. *B*, Cross-sectional overview of SAFOD drilling operations. *C*, Plan-view diagram of SAFOD boreholes relative to the San Andreas Fault at a true vertical depth of approximately 2.7 kilometers. *D*, Cross-sectional diagram of SAFOD boreholes relative to the San Andreas Fault. Parts *C* and *D* show the main borehole and the Phase 3 sidetrack boreholes (Holes E and G). Dashed lines mark the limits of the San Andreas Fault damage zone, defined by low seismic velocities, which lies a few tens of meters northeast of the Pacific and North American Plate boundary. The positions of the two creeping strands—the central deforming zone (CDZ) and southwest deforming zone (SDZ)—are shown. The CDZ is in the center and the SDZ at the southwest margin of the damage zone. Numbered boxes show the positions of the recovered Phase 3 core samples; cores analyzed in this study are shown in orange. Parts *A* and *B* are modified from Moore (2014), whereas *C* and *D* are modified from Zoback and others (2011). SW, southwest; NE, northeast; ICDP, International Continental Scientific Drilling Program; N. Am., North American; sh., shale; sst., siltstone.

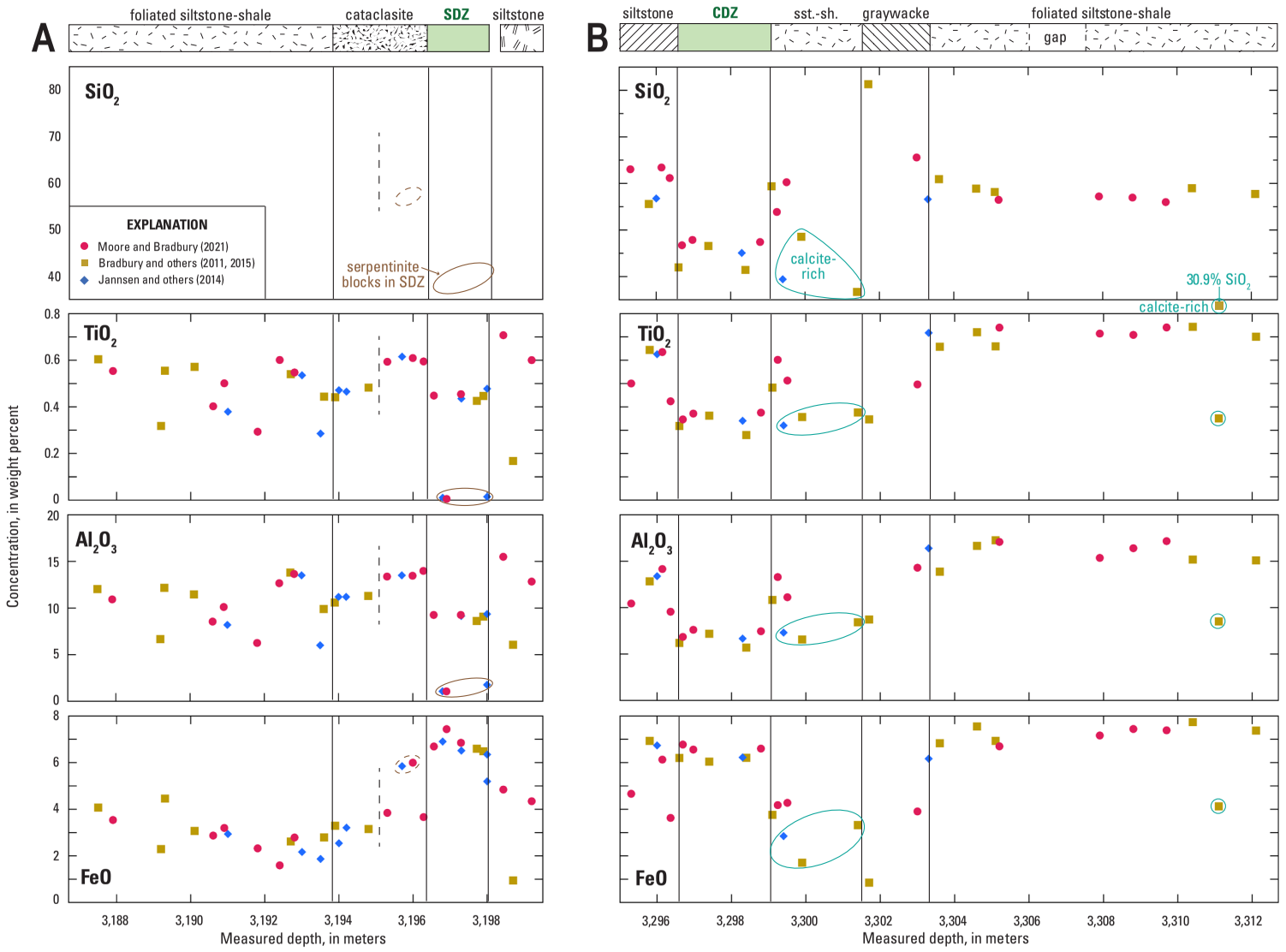

Figure 2. Major element geochemistry of San Andreas Fault Observatory at Depth Hole G core samples, plotted as oxide weight percentages (SiO_2, TiO_2, Al_2O_3, and FeO) relative to depth. *A*, Geochemistry of core section 2 (fig. 1*C, D*), which crosses the southwest deforming zone (SDZ). The cataclasite is separated into two subunits, separated by dashed vertical lines, of somewhat different chemistry. Solid lines encircle compositions for the large serpentinite blocks in the SDZ. Dashed lines encircle two cataclasite samples that are slightly enriched in Mg, Fe, Ni, and Cr, and that are depleted in Si and K. *B*, Geochemistry of core section 3 (fig. 1*C, D*), which crosses the central deforming zone (CDZ). Lines encircle calcite-rich samples; the SiO_2 concentration of the calcite-rich sample at 3,311.1 meters depth in *B* plots below the SiO_2 graph at 30.9 percent. Lithologic sections at top of *A* and *B* are from Bradbury and others (2011). sst.-sh., siltstone-shale.

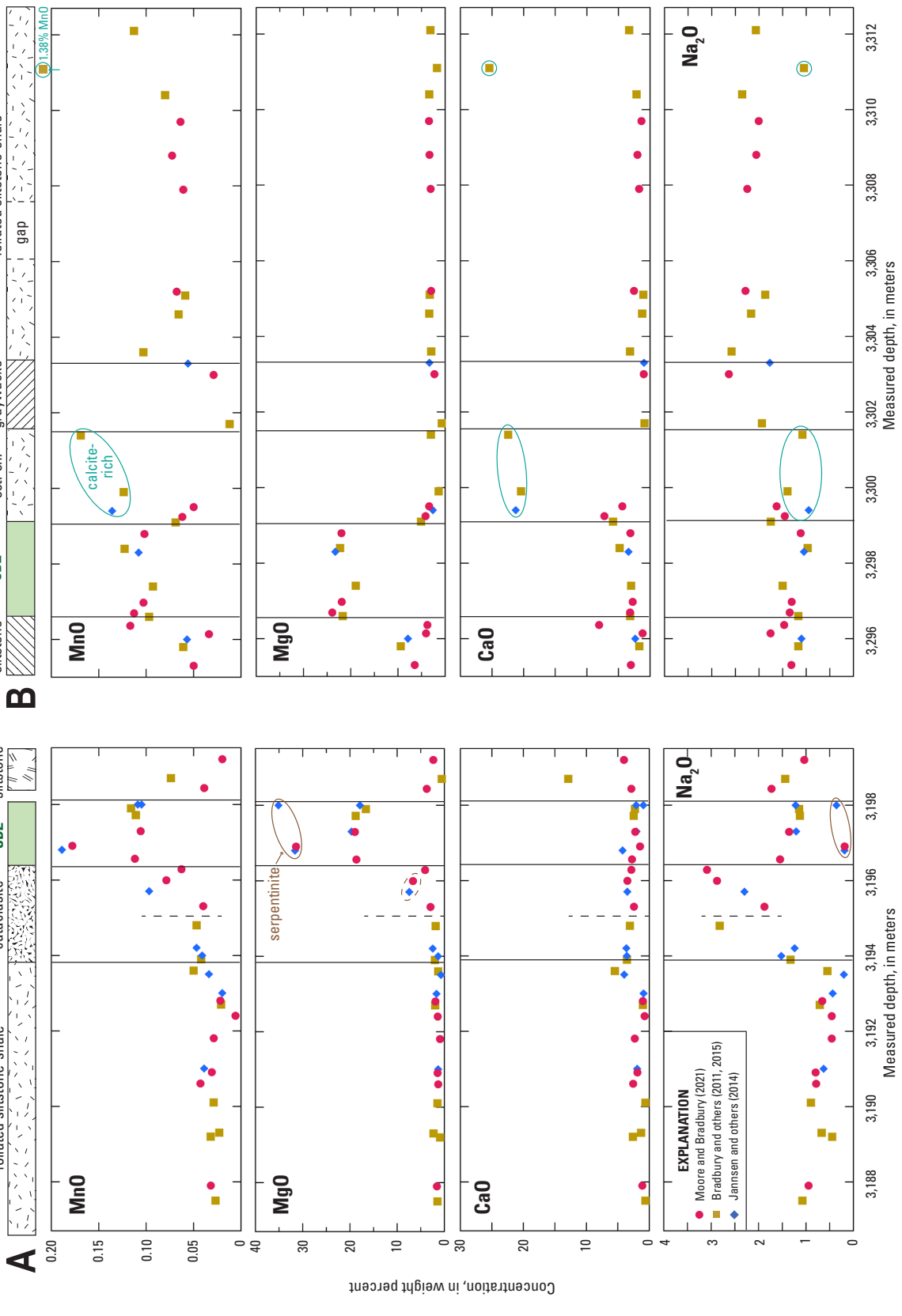

Figure 3. Major element geochemistry of San Andreas Fault Observatory at Depth Hole G core samples, plotted as oxide weight percentages (MnO, MgO, CaO, and Na_2O) relative to depth. *A*, Geochemistry of core section 2 (fig. 1*C*, *D*), which crosses the southwest deforming zone (SDZ). The cataclasite is separated into two subunits, separated by dashed vertical lines, of somewhat different chemistry. Solid lines encircle compositions for the large serpentinite blocks in the SDZ. The dashed line in the MgO plot encircles two cataclasite samples that are slightly enriched in Mg, Fe, Ni, and Cr, and that are depleted in Si and K. *B*, Geochemistry of core section 3 (fig. 1*C*, *D*), which crosses the central deforming zone (CDZ). Solid lines encircle calcite-rich samples; the MnO concentration of the calcite-rich sample at 3,311.1 meters depth in *B* plots above the MnO graph at 1.38 percent. Lithologic sections at top of *A* and *B* are from Bradbury and others (2011). sst.-sh., siltstone-shale.

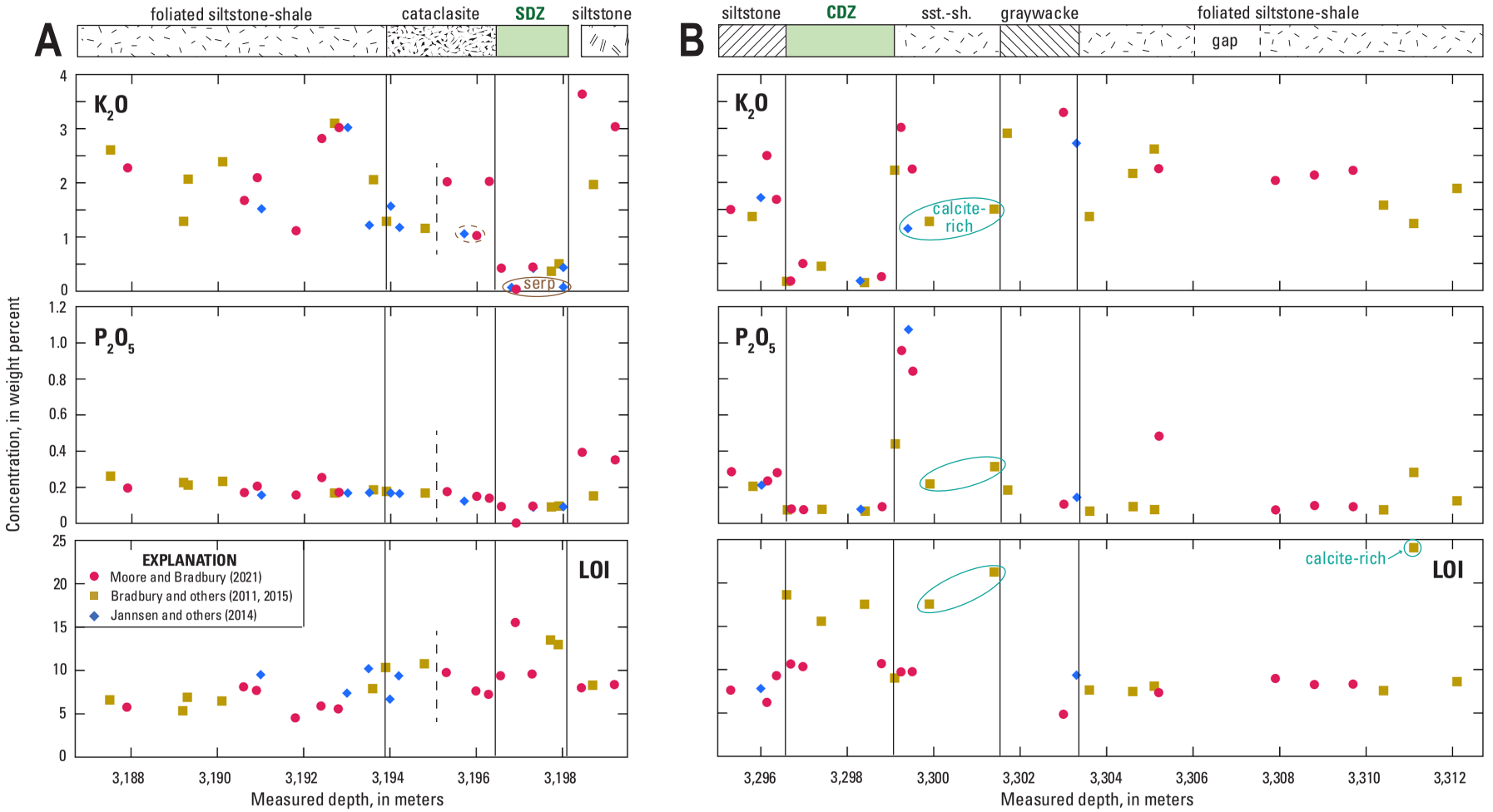

Figure 4. Major element geochemistry of San Andreas Fault Observatory at Depth Hole G core samples, plotted as oxide weight percentages (K_2O and P_2O_5) and loss on ignition (LOI) values relative to depth. *A*, Geochemistry of core section 2 (fig. 1*C, D*), which crosses the southwest deforming zone (SDZ). The cataclasite is separated into two subunits, separated by dashed vertical lines, of somewhat different chemistry. The solid line on the K_2O plot encircles compositions for the large serpentinite blocks in the SDZ. The dashed line in the MgO plot encircles two cataclasite samples that are slightly enriched in Mg, Fe, Ni, and Cr, and that are depleted in Si and K. *B*, Geochemistry of core section 3 (fig. 1*C, D*), which crosses the central deforming zone (CDZ). Solid lines encircle calcite-rich samples. Lithologic sections at top of *A* and *B* are from Bradbury and others (2011). sst.-sh., siltstone-shale, serp, serpentinite.

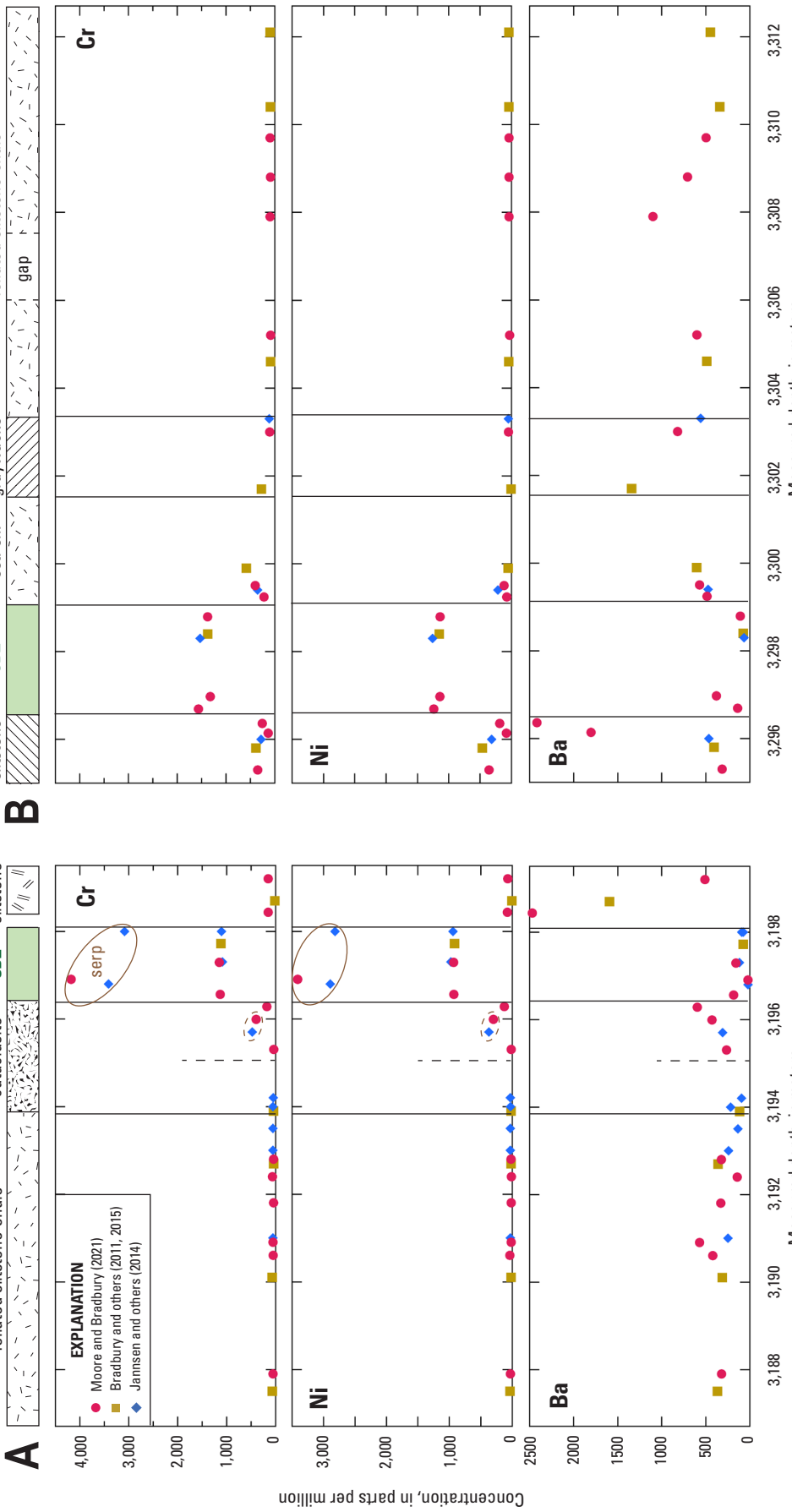

Figure 5. Distribution of the trace elements chromium (Cr), nickel (Ni), and barium (Ba) in San Andreas Fault Observatory at Depth Hole G core samples, plotted in elemental parts per million relative to depth. *A*, Trace element distribution for core section 2 (fig. 1*C*, *D*), which crosses the southwest deforming zone (SDZ). The cataclasite is separated into two subunits, separated by dashed vertical lines, of somewhat different chemistry. Solid lines encircle compositions for the large serpentinite blocks in the SDZ (labeled "serp"). Dashed lines encircle two cataclasite samples that are slightly enriched in Mg, Fe, Ni, and Cr, and that are depleted in Si and K. *B*, Trace element distribution for core section 3 (fig. 1*C*, *D*), which crosses the central deforming zone (CDZ). Lithologic sections at top of *A* and *B* are from Bradbury and others (2011). sst.-sh., siltstone-shale.

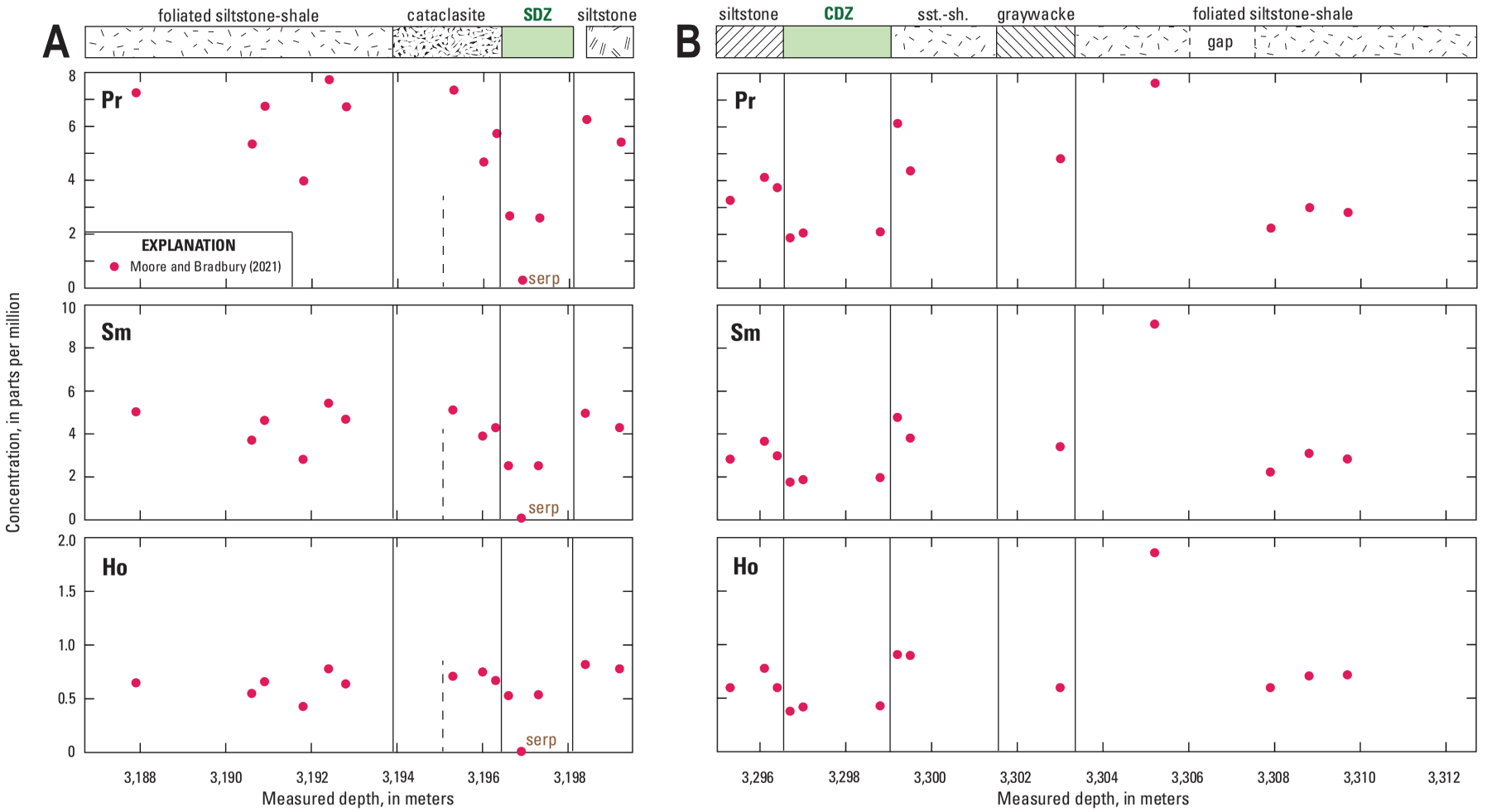

Figure 6. Selected rare earth element concentrations in San Andreas Fault Observatory at Depth Hole G core samples relative to depth: praseodymium (Pr; atomic number [no.] 59), samarium (Sm; atomic no. 62), and holmium (Ho; atomic no. 67). *A*, Rare earth element concentrations in core section 2 (fig. 1*C*, *D*), which crosses the southwest deforming zone (SDZ). The cataclasite is separated into two subunits, separated by dashed vertical lines, of somewhat different chemistry. Points labeled "serp" denote compositions for a large serpentinite block in the SDZ. *B*, Rare earth element concentrations in core section 3 (fig. 1*C*, *D*), which crosses the central deforming zone (CDZ). Lithologic sections at top of *A* and *B* are from Bradbury and others (2011). sst.-sh., siltstone-shale.

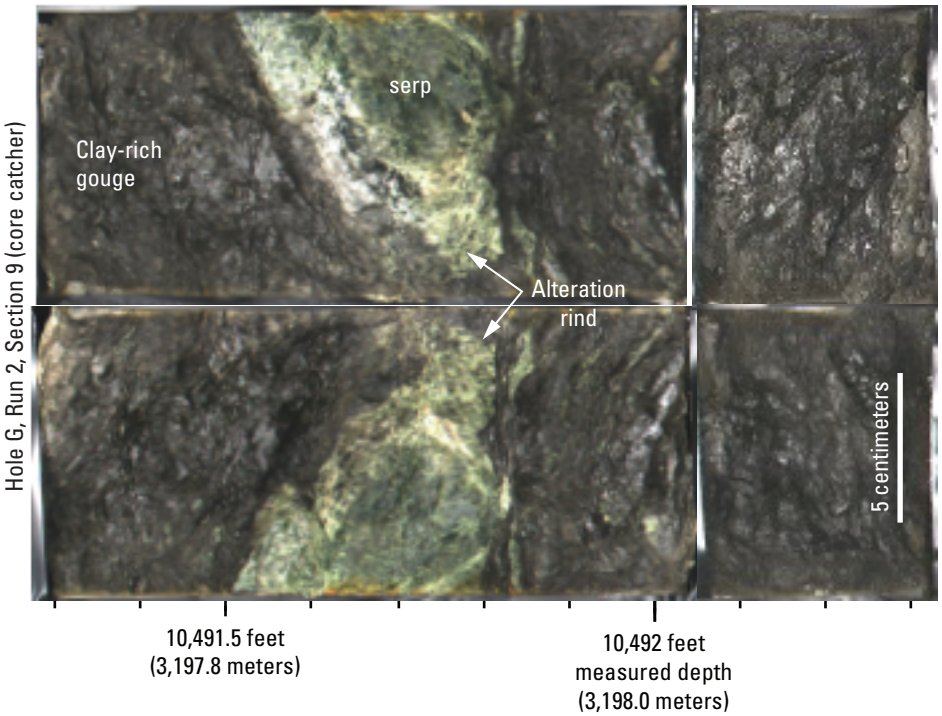

Figure 7. Core photographs showing the northeast end of the southwest deforming zone in the San Andreas Fault Observatory at Depth. The core section split in half upon recovery, revealing the interior of a serpentinite (serp) block at least 9 centimeters long in the magnesium-clay-rich gouge.

The distribution of these new data relative to their locations in the recovered core are plotted in figures 2–6 along with the whole-rock geochemistry data from Bradbury and others (2011, 2015) and Janssen and others (2014). All the major elements and the LOI values are presented in figures 2–4. A small selection of trace and rare earth element data is shown in figures 5 and 6, respectively. It should be noted that Janssen and others (2014) plotted 12 whole-rock compositions in their figure 4, but the table of XRF compositions in their supporting data files contains 13 analyses. The reported depth and chemistry of the additional sample correspond to a serpentinite cobble in the SDZ at ~3,197.9 m depth[3] (fig. 7), providing a third serpentinite data point for comparison with the rest of the core. The sample from Janssen and others (2014) at 3,305.2 m depth coincides with the contact between graywacke and foliated siltstone-shale, so it may be a mix of the two lithologies.

In the next section, we briefly describe some of the notable aspects of the core chemistry revealed in the combined dataset and suggest possible causes for those features.

[3]Core log depths, initially measured in feet, are converted to meters in this report.

Some Aspects of Hole G Core Chemistry

Ultramafic Rock Components of the Central Deforming Zone (CDZ) and Southwest Deforming Zone (SDZ)

The dominant compositional feature of the Hole G core is the large ultramafic contribution to both the CDZ and SDZ and the near-total absence of ultramafic material from the rest of the core (Holdsworth and others, 2011; Bradbury and others, 2011, 2015; Moore and Rymer, 2012; Moore, 2014). The ultramafic material is serpentinite and is interpreted to have been tectonically entrained into the fault from a deep serpentinite source that intersects the fault on the northeast side (McPhee and others, 2004; Moore and Rymer, 2007, 2012). Serpentinite that crops out within the fault zone near the drill site (Nelson Creek locality of Rymer and others [2006]) is largely unaltered, and the exposed northeast contact between the serpentinite and the sedimentary wall rocks is lined with only a thin band of magnesium-clay-rich fault gouge

(Moore and Rymer, 2012). At the higher temperatures and higher confining and fluid pressures of the depth at which the core was recovered (~2.7 km), shearing-enhanced reactions between the ultramafic fault rocks and the crustal wall rocks are much more advanced; the magnesium-rich smectite clays saponite and corrensite predominate in these zones. Details of the metasomatic alteration processes in the CDZ and SDZ were presented by Bradbury and others (2015) and Moore and Rymer (2012). These reactions were duplicated in hydrothermal friction experiments that sheared serpentinite against granite (Moore and Lockner, 2013). The more slowly creeping SDZ contains the largest remnants of serpentinite, including a boulder ~40 centimeters (cm) in diameter near the southwest margin and the previously mentioned ~9-cm cobble (fig. 7) at the northeast end. Two of the three serpentinite compositions come from the interior of the 40-cm block. The serpentinite (circled with solid lines in parts *A* of figures 2–5) has low Si, Al, Ti, Na, and K concentrations, high Mg, Cr, Ni, and LOI concentrations, and the lowest rare earth element concentrations (fig. 6). The bulk chemistry of the SDZ and CDZ gouges is correspondingly enriched or depleted in these same elements compared to the adjacent crustal rock units.

Chemical Exchange Across the Foliated Gouge-Wall Rock Boundaries

Overall, the clay-rich gouge zones act as permeability barriers for cross-fault fluid flow at depth (Wiersberg and Erzinger, 2007, 2008, 2011), and despite marked chemical potential gradients at the gouge-wall rock boundaries, metasomatic exchange by diffusional mass transfer along these contacts is minimal (figs. 2–6). Moore (2014) documented a 0.2-millimeter-wide zone of slight magnesium enrichment and silicon depletion in the cataclasite at the southwest boundary of the SDZ. Some magnesium-rich pore fluids have also entered the wall rocks along microfractures, as evidenced by saponite-lined microcracks that extend as far as ~20 mm into the siltstone southwest of the CDZ (Moore, 2014). The modest enrichment in Mg, Fe, Cr, and Ni and the relative depletion of Si in two cataclasite samples located 0.5–1.0 m from the SDZ (circled with dashed lines in figures 2–5) may also reflect fluid migration into the cataclasite along fractures. The cataclasite contains veins comprising calcite + clays ± zeolites (fig. 8). Smectite clays in a sample from 3,196.1 m depth (fig. 8*A*, *B*) include some saponitic clays similar to those found in the SDZ (Moore, 2014). In contrast, clays in calcite veins (fig. 8*C*) from a sample located ~1 m farther from the SDZ are all mixed-layer illite-smectite clays.

Wall Rock Chemistry

Compositional differences among the lithologic units of sedimentary origin are not as marked as those between the ultramafic-rich gouge zones and the rest of the core. However, some of the units have distinctive chemical features, as described in this section. The two units labeled “foliated siltstone-shale” in figures 2–6, located at the southwest and northeast ends of the Hole G core, span about 7.0 and 9.5 m of the analyzed core, respectively, making them the thickest in these sections. Despite their same designation, they differ somewhat in major element chemistry. The southwest unit has the highest silica concentrations in Hole G (fig. 2), consistent with its high quartz content (fig. 9*A*). This rock unit is also characterized by sample-to-sample variations in the concentrations of titanium, aluminum, potassium, and, to some extent, iron (figs. 2, 4). Felsic volcanic rocks appear to be the main detrital component of the southwest foliated siltstone-shale. The light-colored rock fragments in figure 9*B* consist largely of quartz, potassium feldspar, and plagioclase (fig. 9*C*, *D*). The dark, fine-grained matrix material is more enriched in pyrite, chlorite, and smectite clays compared to lighter regions. The whole-rock geochemistry, therefore, reflects the proportions of lighter and darker materials in a given XRF sample.

Despite considerable textural variations, the northeastern foliated siltstone-shale is generally uniform in its chemistry over the cored interval. Silica concentrations are approximately 10 weight percent lower than in the southwest foliated siltstone-shale, but the northeast unit has the highest aluminum and titanium contents in Hole G and the highest iron concentrations outside the CDZ and SDZ. This combination of elements may reflect relatively high detrital biotite contents, the biotite having since been largely chloritized during diagenesis (fig. 10*A*). A part of the northeast foliated siltstone-shale from 3,309.3 m depth (fig. 10*B*) is shown at progressively higher magnifications in figure 10*B–D*. Most of the bright, irregularly shaped patches in the backscattered electron scanning electron microscope images are chlorite.

The siltstone-shale just northeast of the CDZ is characterized by high calcium and phosphorus concentrations. This rock unit contains many veins and patches of calcite (fig. 11*A*), and about half of its analyzed samples have CaO contents in excess of 20 weight percent, along with elevated MnO contents and LOI values (circled in parts *B* of figures 2–4). Although calcite veining is ubiquitous in the Hole G core, only one other sample (from 3,311.1 m depth) contains more than 20 weight percent CaO and is accompanied by high MnO and LOI contents. The highest phosphorous concentrations (0.85–1.1 weight percent P_2O_5) in the Hole G core are also found in the siltstone-shale adjoining the CDZ. These rocks contain fossil shell fragments that have a distinctive reddish color in plane-polarized light (fig. 11) and are made of calcium phosphate. The fossils are tentatively identified as lingulids, which are brachiopods of the order Lingulida and the only brachiopods that have phosphatic shells. Lingulids live in the same benthic slope environments as the Late Cretaceous fossils identified in the Great Valley sequence core collected from the bottom of the SAFOD main hole (K. McDougall, U.S. Geological Survey, written commun., 2005), although they have existed from the Cambrian to the present.

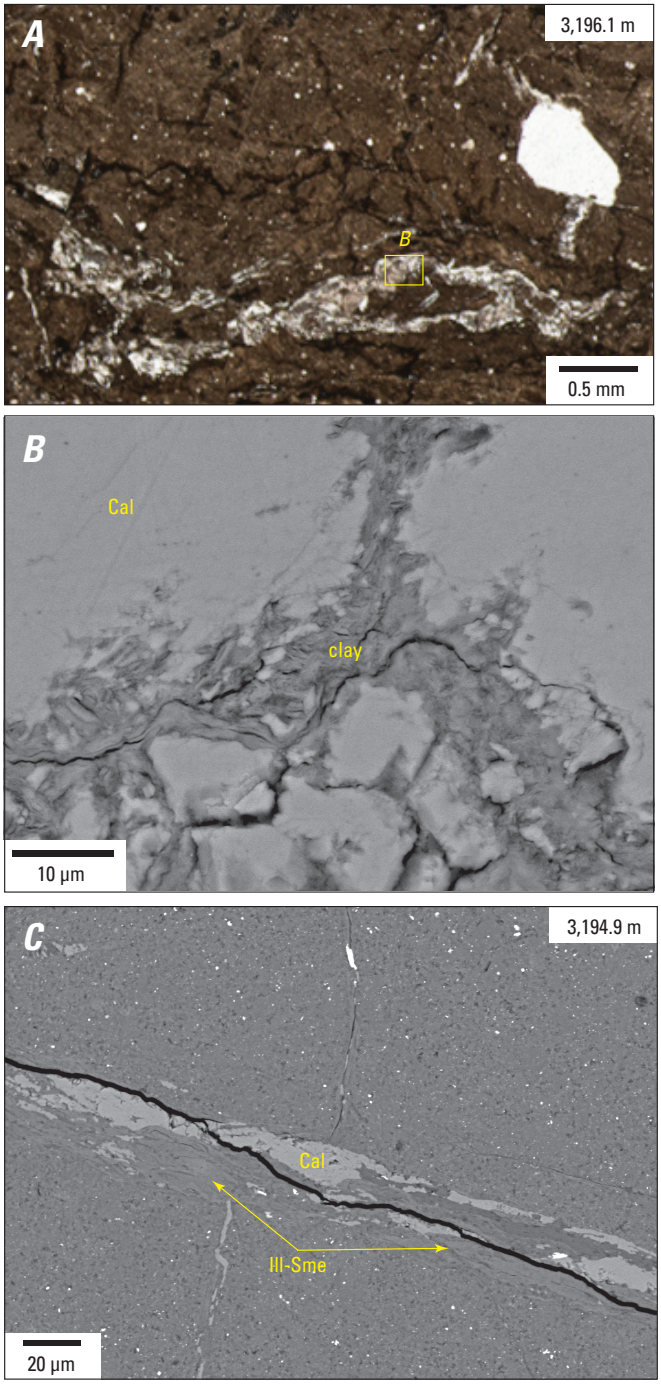

Figure 8. Microscope photographs of calcite veins in the cataclasite of San Andreas Fault Observatory at Depth Hole G. *A*, Plane-polarized light image showing a complexly fractured area at 3,196.1 m depth that largely sealed with calcite, clays, and some zeolites. Box shows area of part *B*. *B*, Backscattered electron (BSE) scanning electron microscope (SEM) image showing saponitic smectite clays intergrown with calcite. *C*, BSE SEM image of a calcite-, clay-, and zeolite-filled vein at 3,194.9 m depth. The clays in this image are relatively low-magnesium illite-smectite clays. Cal, calcite; Ill-Sme, illite-smectite clay; m, meter; mm, millimeter; µm, micrometer.

The cataclasite southwest of the SDZ may have two compositionally distinct subunits of about equal width. The concentrations of several elements, most notably aluminum, titanium, silicon, and potassium, change at ~3,195 m depth (figs. 2–5). Even excluding the possible ultramafic contributions to two of the samples near the SDZ, the silica contents of the two remaining samples in this subunit are slightly lower and the iron and magnesium contents somewhat higher than those on the southwest side. The potassium contents of those two remaining samples are substantially higher than they are in the samples to the southwest. A recent study by Coffey and others (2022) also revealed other differences across the width of the cataclasite. On the basis of thermal maturity measurements of biomarkers in samples across Hole G, they determined that the only values well above background burial heating levels were concentrated in the cataclasite unit, although heating extended a short distance (to ~3,193 m depth) into the foliated siltstone-shale (see also Hadizadeh and Boyle, 2018). The adjoining SDZ gouge showed no evidence of heating. Coffey and others (2022) also measured the youngest potassium-argon ages in the zone of heating, attributing both the biomarker and potassium-argon results to frictional heating accompanying earthquakes. Notably, the biomarker temperatures are on average higher and the ages somewhat older at depths of 3,195 m and greater, approximately coincident with the possible compositional transition marked in figures 2–5.

A comprehensive examination of the cataclasite could help to determine whether or not this apparent compositional division is valid and, if so, if the compositional differences are of sedimentary (for example, detrital or diagenetic) origin or are the product of faulting processes, such as the many earthquakes postulated by Coffey and others (2022). Detailed investigations of this cataclasite are extremely limited. A single sample at ~3,194 m depth was featured in five studies dealing separately with clay fabrics (Wenk and others, 2010; Janssen and others, 2012), amorphous material (Janssen and others, 2010), nanoporosity (Janssen and others, 2011), and deformation features in calcite veins (Rybacki and others, 2011). A study by Hadizadeh and Boyle (2018), carried out on a single sample located just southwest of the cataclasite, focused on pyrite and calcite microstructures.

Finally, four samples have elevated barium contents (greater than 1,500 parts per million): two from the siltstone northeast of the SDZ and two from the siltstone southwest of the CDZ (fig. 5). Of these, one pair is natural whereas the other pair may denote contamination by drilling mud. The detrital potassium feldspar in the siltstone northeast of the SDZ contains barium, some of which has exsolved to form discontinuous rims of barite ($BaSO_4$) around the feldspar clasts (fig. 12*A*). This barite typically contains modest to moderate amounts of the strontium end member celestine ($SrSO_4$) (fig. 12*B*). The drilling mud used for Phase 3 coring operations was a fine-grained rock powder of approximately granitic mineralogy with added barite. During coring operations, some of the mud was injected into the core along the

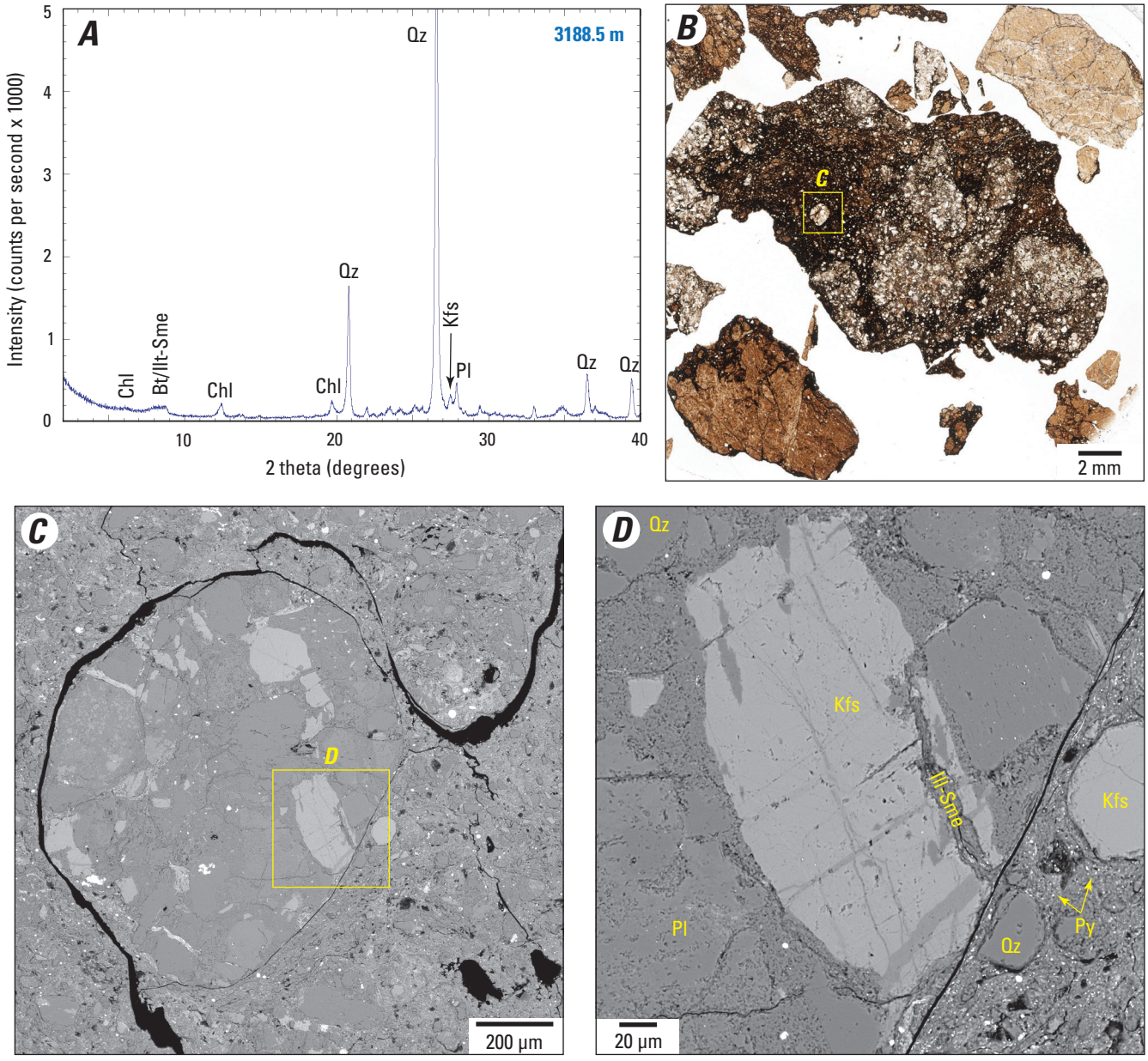

Figure 9. X-ray diffraction (XRD) data from and microscope images of the quartz-rich foliated siltstone-shale at the southwest end of San Andreas Fault Observatory at Depth Hole G. *A*, Representative XRD pattern for the siltstone-shale, sampled at 3,188.5 m depth. *B*, Thin section photograph of rock fragments from a sample at 3,187.3 m depth, obtained for laboratory friction experiments (Lockner and others, 2011). Box shows area of part *C*. *C*, Backscattered electron (BSE) scanning electron microscope (SEM) image showing a clast of volcanic-rich detritus in a dark, fine-grained matrix. Box shows area of part *D*. *D*, BSE SEM image showing a closer view of the clast-matrix boundary. Chl, chlorite; Bt, biotite, Ilt-Sme, illite-smectite clay; Qz, quartz; Kfs, potassium feldspar; Pl, plagioclase; Py, pyrite; m, meter; mm, millimeter; µm, micrometer.

contact between the gouge and wall rock (Moore, 2014). The siltstone unit southwest of the CDZ is substantially fractured along a centimeter-scale zone at the contact. Several of those fractures are propped open with the drilling mud (fig. 12*C*), which contains barite characterized by low strontium content (fig. 12*D*). The two high-barium siltstone samples are those located closest to the contact with the CDZ. Although the overall granitic mineralogy of the drilling mud might be difficult to distinguish from the wall rock geochemistry, the low-strontium barite additive makes it possible to identify minor drilling mud contamination in those samples.

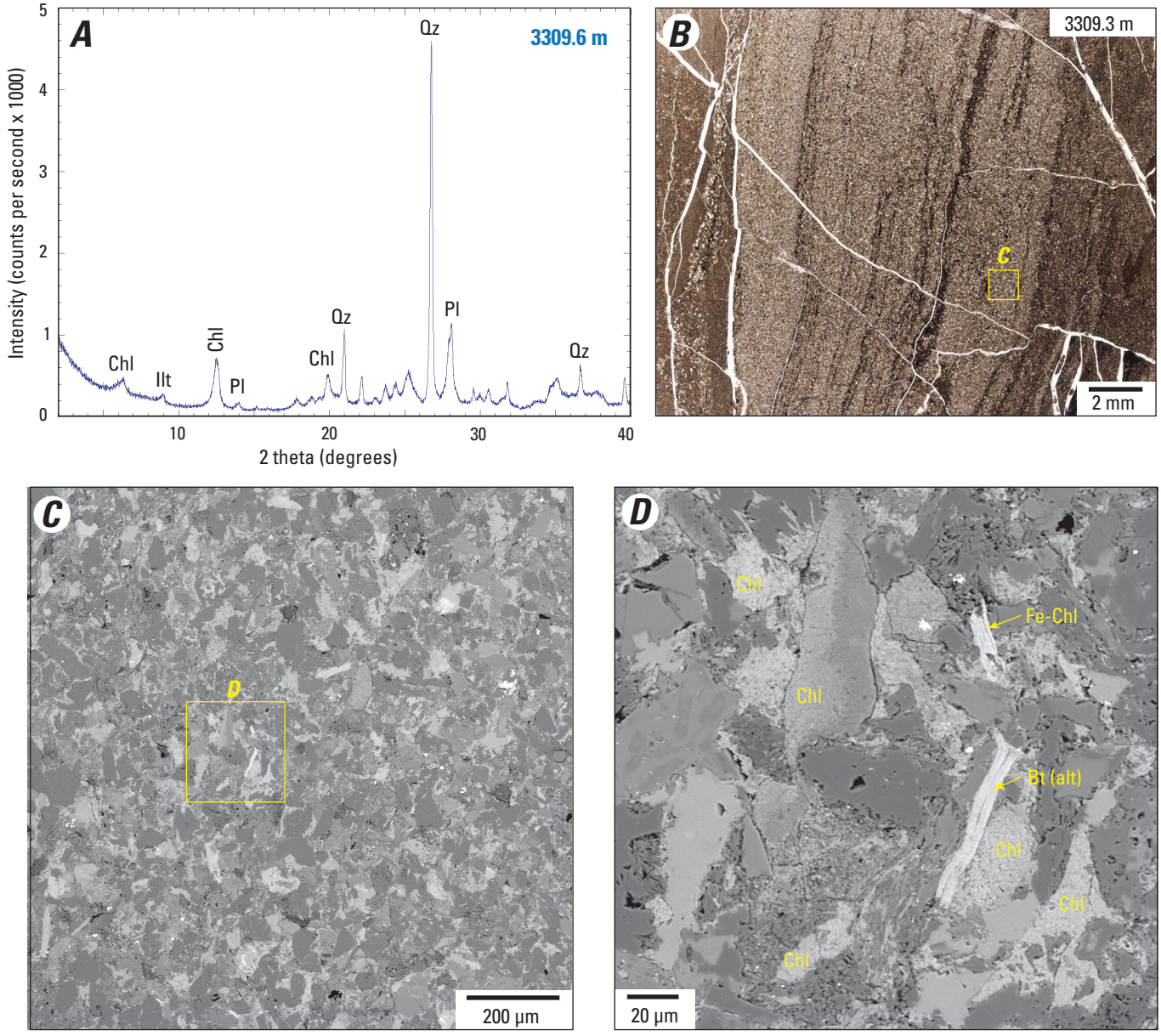

Figure 10. X-ray diffraction (XRD) data from and microscope images of the chlorite-rich foliated siltstone-shale from San Andreas Fault Observatory at Depth core at the northeast end of Hole G. *A*, Plot of the XRD pattern for the foliated siltstone-shale, sampled at 3,309.6 m depth. *B*, Thin section photograph of the siltstone, sampled at 3,309.3 m depth, used to measure permeability (Morrow and others, 2014). Box shows area of part *C*. *C*, Backscattered electron (BSE) scanning electron microscope (SEM) image. Box shows area of part *D*. *D*, BSE SEM image. Parts *C* and *D* show the widespread distribution of bright patches of chloritized biotite in the siltstone. The bright color reflects their high iron contents. Chl, chlorite; Ilt, illite; Pl, plagioclase; Qz, quartz; Fe-Chl, iron-rich chlorite; Bt, biotite; alt, altered; m, meter; mm, millimeter; µm, micrometer.

Concluding Remarks

The expanded XRF geochemical dataset reveals a number of compositional variations across the length of the SAFOD Hole G core. A few distinctive chemical features of individual units that can be readily tied to their mineral ± fossil assemblages are highlighted in this report. The whole-rock geochemistry may also be useful for evaluating possible earthquake-induced deformation processes in the core southwest of the SDZ or for determining whether some elements have been preferentially concentrated in, or removed from, the CDZ and SDZ as a result of reaction or solution-transfer processes.

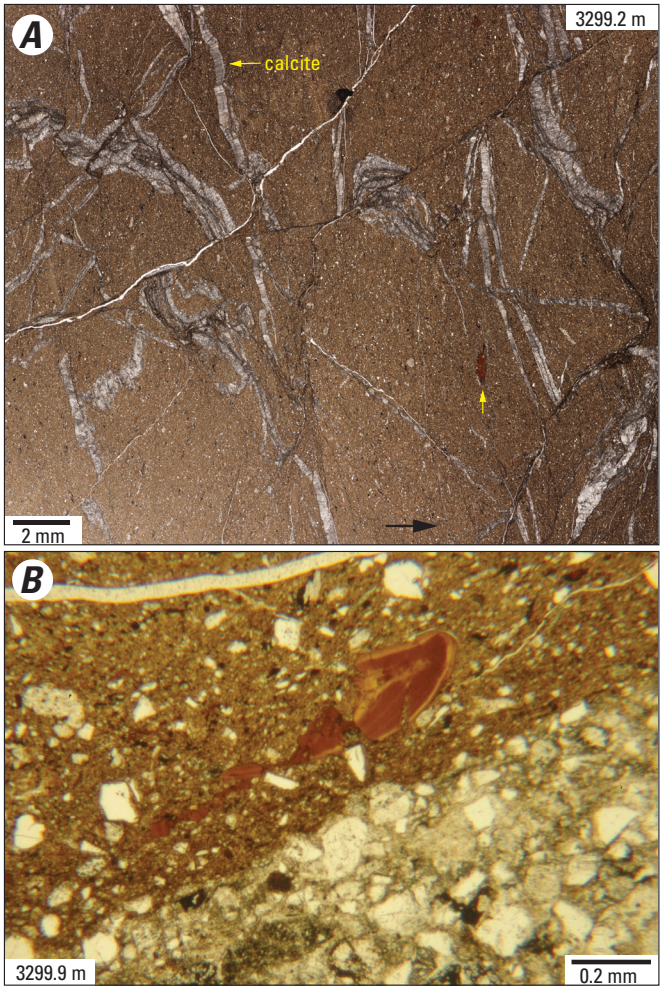

Figure 11. Thin section photographs of the siltstone-shale adjoining the northeast side of the central deforming zone (sampled from San Andreas Fault Observatory at Depth Hole G). *A*, Photograph from 3,299.2 m depth showing extensive calcite veining, which produces high calcium concentrations in several samples from this unit. A dark red fossil shell fragment is visible in the lower right quadrant. The black arrow points in the up direction of the core sample. *B*, Photograph from 3,299.9 m depth showing a fragmented, dark red fossil shell. m, meter; mm, millimeter.

References Cited

Bradbury, K.K., Davis, C.R., Shervais, J.W., Janecke, S.U., and Evans, J.P., 2015, Composition, alteration, and texture of fault-related rocks from Safod core and surface outcrop analogs—Evidence for deformation processes and fluid-rock interactions: Pure and Applied Geophysics, v. 172, no. 5, p. 1053–1078, https://doi.org/10.1007/s00024-014-0896-6.

Bradbury, K.K., Evans, J.P., Chester, J.S., Chester, F.M., and Kirschner, D.L., 2011, Lithology and internal structure of the San Andreas Fault at depth based on characterization of Phase 3 whole-rock core in the San Andreas Fault Observatory at Depth (SAFOD) borehole: Earth and Planetary Science Letters, v. 310, no. 1–2, p. 131–144,https://doi.org/10.1016/j.epsl.2011.07.020.

Coffey, G.L., Savage, H.M., Polissar, P.J., Cox, S.E., Hemming, S.R., Winckler, G., and Bradbury, K.K., 2022, History of earthquakes along the creeping section of the San Andreas fault, California, USA: Geology, v. 50, no. 4, p. 516–521, https://doi.org/10.1130/G49451.1.

Hadizadeh, J., and Boyle, A.P., 2018, A study of secondary pyrite deformation and calcite veins in SAFOD damage zone with implications for aseismic creep deformation mechanism at depths >3 km: Journal of Structural Geology, v. 117, p. 14–26, https://doi.org/10.1016/j.jsg.2018.09.005.

Holdsworth, R.E., van Diggelen, G.W.E., Spiers, C.J., de Bresser, J.H.P., Walker, R.J., and Bowen, L., 2011, Fault rocks from the SAFOD core samples—Implications for weakening at shallow depths along the San Andreas Fault, California: Journal of Structural Geology, v. 33, no. 2, p. 132–144. https://doi.org/10.1016/j.jsg.2010.22.010.

Janssen, C., Kanitpanyacharoen, W., Wenk, H.-R., Wirth, R., Morales, L., Rybacki, E., Kienast, M., and Dresen, G., 2012, Clay fabrics in SAFOD core samples: Journal of Structural Geology, v. 43, p. 118–127, https://doi.org/10.1016/j.jsg.2012.07.004.

Janssen, C., Wirth, R., Reinicke, A., Rybacki, E., Naumann, R., Wenk, H.-R., and Dresen, G., 2011, Nanoscale porosity in SAFOD core samples (San Andreas Fault): Earth and Planetary Science Letters, v. 301, no. 1–2, p. 179–189, https://doi.org/10.1016/j.epsl.2010.10.040.

Janssen, C., Wirth, R., Rybacki, E., Naumann, R., Kemnitz, H., Wenk, H.-R., and Dresen, G., 2010, Amorphous material in SAFOD core samples (San Andreas Fault)—Evidence for crush-origin pseudotachylytes?: Geophysical Research Letters, v. 37, no. 1, article L01303, 6 p., https://doi.org/10.1029/2009GL040993.

Janssen, C., Wirth, R., Wenk, H.-R., Morales, L., Naumann, R., Kienast, M., Song, S.-R., and Dresen, G., 2014, Faulting processes in active faults—Evidences from TCDP and SAFOD drill core samples: Journal of Structural Geology, v. 65, p. 100–116, https://doi.org/10.1016/j.jsg.2014.04.004.

Lockner, D.A., Morrow, C., Moore, D., and Hickman, S., 2011, Low strength of deep San Andreas fault gouge from SAFOD core: Nature, v. 472, p. 82–85, https://doi.org/10.1038/nature09927.

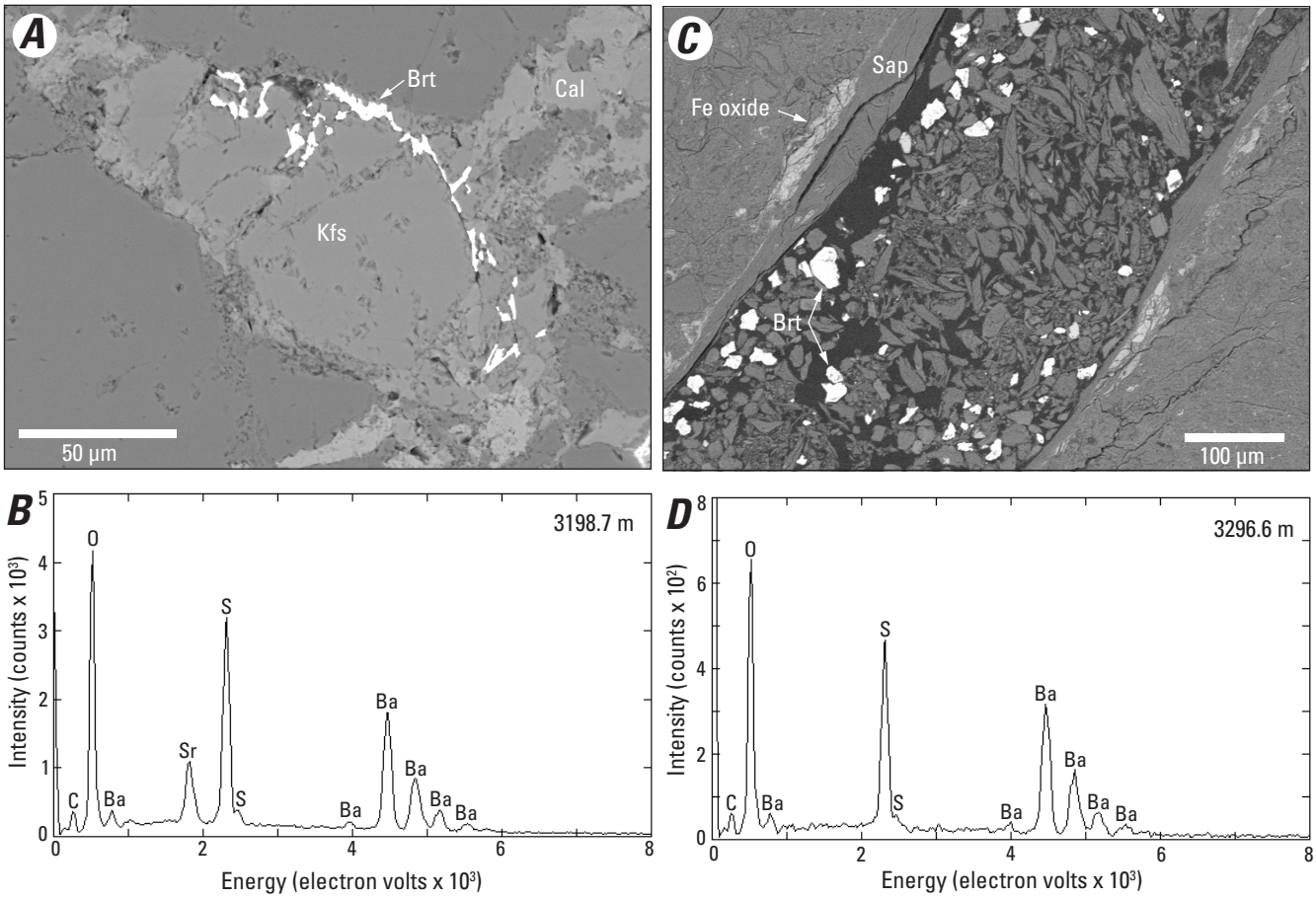

Figure 12. Microscope images and energy-dispersive X-ray spectroscopy (EDS) plots showing sources of barium in the core sampled from San Andreas Fault Observatory at Depth Hole G. *A*, Backscattered electron (BSE) scanning electron microscope (SEM) image of a potassium feldspar clast rimmed by exsolved barite ($BaSO_4$) in the siltstone northeast of the southwest deforming zone (at 3,198.7 m depth). *B*, EDS spectrum of the barite from *A*, showing it is rich in the strontium end member celestine ($SrSO_4$). *C*, BSE SEM image of a saponite-filled veinlet in siltstone, located about 5 millimeters southwest of the central deforming zone boundary at 3,296.6 m depth. The veinlet has been propped open with drilling mud consisting of granitic rock flour augmented with barite. *D*, EDS spectrum of the barite from *C*, showing that the drilling-mud-additive barite typically contains little or no strontium. Brt, barite; Cal, calcite; Kfs, potassium feldspar; Fe, iron; Sap, saponite; C, carbon; O, oxygen; Ba, barium; Sr, strontium; S, sulfur; µm, micrometer; m, meter.

McPhee, D.K., Jachens, R.C., and Wentworth, C.M., 2004, Crustal structure across the San Andreas Fault at the SAFOD site from potential field and geologic studies: Geophysical Research Letters, v. 31, no. 12, article L12S03, 4 p, https://doi.org/10.1029/2003GL019363.

Moore, D.E., 2014, Comparative mineral chemistry and textures of SAFOD fault gouge and damage-zone rocks: Journal of Structural Geology, v. 68, part A, p. 82–96, https://doi.org/10.1016/j.jsg.2014.09.002.

Moore, D.E., and Bradbury, K.K., 2021, Whole-rock chemistry of Hole G core samples from the San Andreas Fault Observatory at Depth (SAFOD), California: U.S. Geological Survey data release, https://doi.org/10.5066/P9ZVZXOK.

Moore, D.E., and Lockner, D.A., 2013, Chemical controls on fault behavior—Weakening of serpentinite sheared against quartz-bearing rocks and its significance for fault creep in the San Andreas system: Journal of Geophysical Research, Solid Earth, v. 118, no. 5, p. 2558–2570, https://doi.org/10.1002/jgrb.50140.

Moore, D.E., and Rymer, M.J., 2007, Talc-bearing serpentinite and the creeping section of the San Andreas fault: Nature, v. 448, p. 795–797,https://doi.org/10.1038/nature06064.

Moore, D.E., and Rymer, M.J., 2012, Correlation of clayey gouge in a surface exposure of serpentinite in the San Andreas Fault with gouge from the San Andreas Fault Observatory at Depth: Journal of Structural Geology, v. 38, p. 51–60, https://doi.org/10.1016/j.jsg.2011.11.014.

Morrow, C.A., Lockner, D.A., Moore, D.E., and Hickman, S., 2014, Deep permeability of the San Andreas Fault from San Andreas Fault Observatory at Depth (SAFOD) core samples: Journal of Structural Geology, v. 64, p. 99–114, https://doi.org/10.1016/j.jsg.2013.09.009.

Rybacki, E., Janssen, C., Wirth, R., Chen, K., Wenk, H.-R., Stromeyer, D., and Dresen, G., 2011, Low-temperature deformation in calcite veins of SAFOD core samples (San Andreas Fault)—Microstructural analysis and implications for fault rheology: Tectonophysics, v. 509, no. 1–2, p. 107–119, https://doi.org/10.1016/j.tecto.2011.05.014.

Rymer, M.J., Tinsley, J.C., III, Treiman, J.A., Arrowsmith, J.R., Clahan, K.B., Rosinski, A.M., Bryant, W.A., Snyder, H.A., Fuis, G.S., Toké, N.A., and Bawden, G.W., 2006, Surface fault slip associated with the 2004 Parkfield, California, earthquake: Bulletin of the Seismological Society of America, v. 96, no. 4B, p. S11–S27, https://doi.org/10.1785/0120050830.

Titus, S.J., DeMets, C., and Tikoff, B., 2006, Thirty-five-year creep rates for the creeping segment of the San Andreas Fault and the effects of the 2004 Parkfield earthquake—Constraints from alignment arrays, continuous global positioning system, and creepmeters: Bulletin of the Seismological Society of America, v. 96, no. 4B, p. S250–S268, https://doi.org/10.1785/0120050811.

Titus, S.J., Dyson, M., DeMets, C., Tikoff, B., Rolandone, F., and Bürgmann, R., 2011, Geologic versus geodetic deformation adjacent to the San Andreas fault, central California: Geological Society of America Bulletin, v. 123, no. 5–6, p. 794–820, https://doi.org/10.1130/B30150.1.

Wenk, H.-R., Kanitpanyacharoen, W., and Voltolini, M., 2010, Preferred orientation of phyllosilicates—Comparison of fault gouge, shale, and schist: Journal of Structural Geology, v. 32, no. 4, p. 478–489, https://doi.org/10.1016/j.jsg.2010.02.003.

Wiersberg, T., and Erzinger, J., 2007, A helium-isotope cross-section study through the San Andreas Fault at seismogenic depths: Geochemistry, Geophysics, Geosystems, v. 8, no. 1, article Q01002, 12 p, https://doi.org/10.1029/2006GC001388.

Wiersberg, T., and Erzinger, J., 2008, Origin and spatial distribution of gas at seismogenic depths of the San Andreas Fault from drill-mud analysis: Applied Geochemistry, v. 23, no. 6, p. 1675–1690, https://doi.org/10.1016/j.apgeochem.2008.01.012.

Wiersberg, T., and Erzinger, J., 2011, Chemical and isotopic compositions of drilling mud gas from the San Andreas Fault Observatory at Depth (SAFOD) boreholes—Implications on gas migration and the permeability structure of the San Andreas Fault: Chemical Geology, v. 284, no. 1–2, p. 148–159, https://doi.org/10.1016/j.chemgeo.2011.02.016.

Zoback, M., Hickman, S., and Ellsworth, W., 2010, Scientific drilling into the San Andreas fault zone: Eos, Transactions, American Geophysical Union, v. 91, no. 22, p. 197–199, https://doi.org/10.1029/2010EO220001.

Zoback, M., Hickman, S., and Ellsworth, W., 2011, Scientific drilling into the San Andreas Fault Zone—An overview of SAFOD's first five years: Scientific Drilling, v. 11, p. 14–28, https://doi.org/10.5194/sd-11-14-2011.

Moffett Field and Reston Publishing Service Centers
Manuscript approved February 23, 2023
Edited by Claire E. Ashcraft
Illustrative support by Cory Hurd
Layout by Ethan Whitecotton

ISSN 2331-1258 (online)
https://doi.org/10.3133/ofr20231019